Visual Abstract

Investigation into effective mechanical properties of porous material produced by the additive manufacturing method

Seyed Mohammad Javad Tabatabaee, Mahdi Fakoor
Faculty of New Sciences and Technologies, University of Tehran, Tehran, Iran
mfakoor@ut.ac.ir, smj.tabatabaee@ut.ac.ir

ABSTRACT. Porous materials are defined as materials that contain holes, voids, or spaces in their structures, which can be interconnected or isolated. In the most complex forms of these materials, the holes can have irregular shapes with a random distribution in size, location, and direction, making studying their properties a challenging problem. Additive manufacturing techniques offer opportunities to create complex structures, and in this paper, we investigate the effective mechanical properties of porous material produced by the Fused Displacement Modeling (FDM) technique. We also propose an algorithm for generating a porous body containing irregularly shaped holes with arbitrary distributions in size and location while maintaining specific porosity. Due to the orthotropic properties of bodies created by the FDM technique, Reinforced Isotropic Solid Modeling (RISM) is combined with existing theories that calculate the effective properties of isotropic materials. For the experiments, some modified standard specimen with a porosity of 0.05 to 0.40 has been fabricated, and the elastic modulus and ultimate stress have been calculated using the tensile test. Finally, the results are compared with experimental data.

KEYWORDS. Porous material, Additive manufacturing, Reinforced isotropic material, Effective properties.

OPEN ACCESS

Citation: Tabatabaee, M., Fakoor, M., Investigation into effective mechanical properties of porous material produced by the additive manufacturing method, Frattura ed Integrità Strutturale, 65 (2023) 208-223.

Received: 26.04.2023
Accepted: 02.06.2023
Online First: 10.06.2023
Published: 01.07.2023

INTRODUCTION

Porous materials are a class of materials characterized by their complex internal structure, consisting of a network of interconnected or isolated pores or voids. The porous structure can be formed by a random distribution of pores, resulting in a wide range of pore sizes and shapes. Due to their properties, porous materials are essential in various biological, environmental, energy, and manufacturing applications [1–3].One of the aspects of these materials that have been focused on in this paper is their unique mechanical properties which can enhance or even control the structural components' mechanical properties and their performance. These materials can be designed to exhibit desirable mechanical properties, such as high strength-to-weight ratio, impact resistance, and energy absorption, making them suitable for various structural

applications in mechanical engineering, such as developing lightweight structural components for automobiles and aircraft which can lead to improved fuel efficiency, reduced emissions, and increased safety.
Porous materials have been investigated in various fields for phenomena such as fatigue and failure. However, a comprehensive understanding of their mechanical behavior and the impact of voids on such behavior requires prior identification [4–6]. Establishing a unified quantitative relation that can estimate the effective properties of porous materials based on the relative size and topology of their pore structure remains a subject of an ongoing investigation. Several studies have been done to investigate the mechanical properties of porous materials. One early work by Sokokhod is theoretically investigating the elastic moduli and relative conductivity of powder and fiber porous bodies at different porosity [7]. O'Connell and Budiansky used self-consistent scheme for estimating effective elastic properties of porous bodies containing randomly distributed flat cracks. They proposed effective mechanical properties relation as a function of porosity by assuming that microcracks are circular or elliptical [8]. Horii and Nemat-Nasser calculated the effective mechanical properties of the solid containing microcracks that may be closed or may undergo frictional sliding. The effects of crack closure and load-induced anisotropy are considered in their work [9]. The results were similar to those of O'Connell and Budiansky when all cracks were opened. Sevostianov and Kushch numerically investigated the effect of the pores' distributions on the overall properties of porous materials. The pores were circular and distributed randomly, with porosity up to 0.5 [10]. An analytical homogenization method was developed by Chakraborty to calculate the mechanical properties of fluid-filled porous materials with periodic microstructures [11].
In the investigation of porous materials, the significance of their topology is just as crucial as other aspects of these materials. Quintanilla and Torquato developed an algorithm to create the geometry of a two-phase system containing fully penetrable spheres, which are distributed non-uniformly and tend to cluster [12]. Kushch et al. also described growing particles' molecular dynamics (MD) algorithm to use in computer simulation of progressive damage in fiber-reinforced composite (FRC) materials [13]. algorithms Most of the existing ones use circular and elliptical pores. Still, in this work, we develop an algorithm to generate modified elliptic pores that were randomly deformed and then create porous geometries by these pores with random desaturation in size, location, and orientation for required porosities.
Also, Numerous experiments have been conducted to investigate the behavior of porous materials. Christensen et al. drove isotropic failure that can be applied to low-density porous materials. They used polyvinylchloride foam and executed stress-strain responses in tension, compression, and shear [14]. In another work, Isaksson et al. estimate the approximate micro-strain field of porous material using the images obtained by X-ray computed tomography (CT-scan) of the small wood specimen [15]. The distribution of the pores in specimens is typically uncontrollable because the generation of complex geometries with common manufacturing methods is too complicated or even impossible. But, with additive manufacturing, it's possible to fabricate this complicity. These methods are currently used in many fields, such as aerospace engineering, automotive, food, and engineering industries [16,17]. Because of the cost efficiency and reproduction ability, additive manufacturing is a good choice for prototypes. There are several types of additive manufacturing processes, such as Stereolithography (SLA), Selective Laser Sintering (SLS), Binder Jetting, Direct Energy Deposition (DED), and Fused Deposition Modeling (FDM) [18]. Here we use FDM technology to fabricate our specimens with complex geometry and in different porosities. The body produced by the FDM technique has orthotropic behaviors. In similar works, the materials were typically assumed to be isotropic, and there was no actual control over the properties of the pore. Using FDM technology prepares this opportunity for us to investigate the mechanical properties of porous orthotropic materials more accurately. Combining the RIS (Reinforced Isotropic Solid) theory with the existing effective properties relationship and defining a new RVE, we represent the modified formulation that describes the orthotropic porous body's effective mechanical properties. The result was validated with the experimental test of the new specimens fabricated based on the new porous geometry generating algorithm developed in this work.

EXPERIMENTAL APPROACH

The algorithm for the porous material generation

One of the primary purposes of this work is to generate a geometry with a random distribution of size, shape, and location of holes with specific porosity. Several studies have been done to produce a porous geometry with a random distribution of size and location of the holes, but the holes typically are circular or elliptical; on the other hand, the generation of a general code to create a porous geometry with random shape holes is a complex problem or even impossible if the correct assumption wasn't made. In this work, we assume that the holes are deformed elliptic. So, a MATLAB code was developed to deform an ellipse with a controlled aspect ratio. At first, an ellipse is randomly discrete to

a specific number of equal parts. In each section, a random point on the ellipse's perimeter is determined. These points are moved randomly through an imaginary line that connects the ellipse's center to the points inside or outside (see Fig. 1).

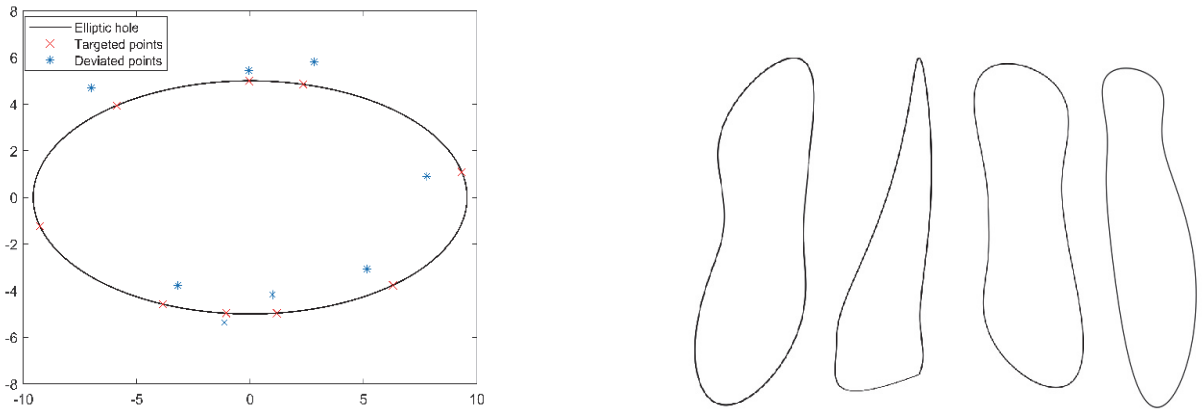

a. ellipse deformation algorithm b. example of the holes in the library

Figure 1: Random shape holes' generation.

After the disposition points are determined, the closed spline generate based on these points, the splines are improved with curve smooth methods, and the curvature and tangency of the splines are checked. To reduce the complexity of the generation of the porous geometry in this work, we generate a library of holes instead of generating a new hole in each segment. This work reduced the calculation cost because all the deformed ellipses are unsuitable, and a fine spline may not be generated with output holes. All the splines in the library check with CAD software to ensure their feasibility, and all the holes in the library are optimized to have the same and specific area to be suitable in the next step. Some of these holes are shown in Fig. 1. b. The aspect ratio of the ellipse was in the range of 7 to 14, and they deviated in intervals 5 and 8 randomly. The deviation factor is 0.1, which means each point will move 0.1 distance between the point and center inside or outside. In this work, 150 holes generate and stored in the library to be used in the following steps.

To generate a porous geometry, another MATLAB code is developed. The purpose of this code is to add new holes to the given body and continue this work to reach determined porosities. In this work, we assume two main rules; first, two neighbor holes always have at least a small distance, i.e., no intersection holes are allowed. The second rule is that hole not allow to intersect with the border of the body so the body has no imperfect hole. Also, to reduce the calculation time, an assumption was made based on the meshing method used in the Finite Element Method (FEM) and Finite Difference Method (FDM) for the location of the pores. Using a length parameter, the body is discrete into smaller parts, and we assume that the center of the pores can only be placed on the corner of these parts. The main parameters in this code are the shape and dimension of the body, the length parameter for meshing, the values of porosity for output, the maximum and minimum length of the holes, the minimum allowable spacing that is also known as impenetrability parameter, the number of allowable trying for rotation of the hole and number of allowable trial and error for one hole. The last input is nodes of the holes in the library that are generated by the first code. These nodes are obtained from the perimeter of the deformed ellipse because using the cad file will add unnecessary complexity to the code. The higher number of nodes will increase the calculation accuracy and time cost.

a. circular body with a volume fraction of 0.25 b. random body with a volume fraction of 0.15

Figure 2: Two examples of MATLAB code output for generation porous body with a random distribution of holes in shape, size, location, and orientation.

After all these parameters are collected, the body will mesh, and the node for the centers will create. Then one of these nodes will be chosen randomly, and after that, one of the holes in the library will select. At first, a random size was assigned to this hole. Then the unit circle is discrete to the number of allowable trying for rotation, and this angle will sort randomly. The selected hole will be placed with these randomly sorted angles, and if the two main rules are satisfied, this hole will be accepted, the angle try will be stopped, and all the mesh nodes inside the hole will be deleted. But if all the angles fail, two situations will happen. First, if any trial and error opportunity is left for the hole, the size will reduce; for the last try case, it will become the minimum size. And if the hole can't fit even with the minimum size, the hole can't fit, another hole will be randomly selected, and this procedure will continue until one hole can satisfy all the rules or all holes fail. In the case of all failure, the node will remove from the body to prevent the reselection. The outputs of this code are the hole's number, the location of the holes, their scale factor, and their rotation angle. Fig. 2 shows some examples of the output with the second hole, and Fig. 3 describes the flowchart of the second code.

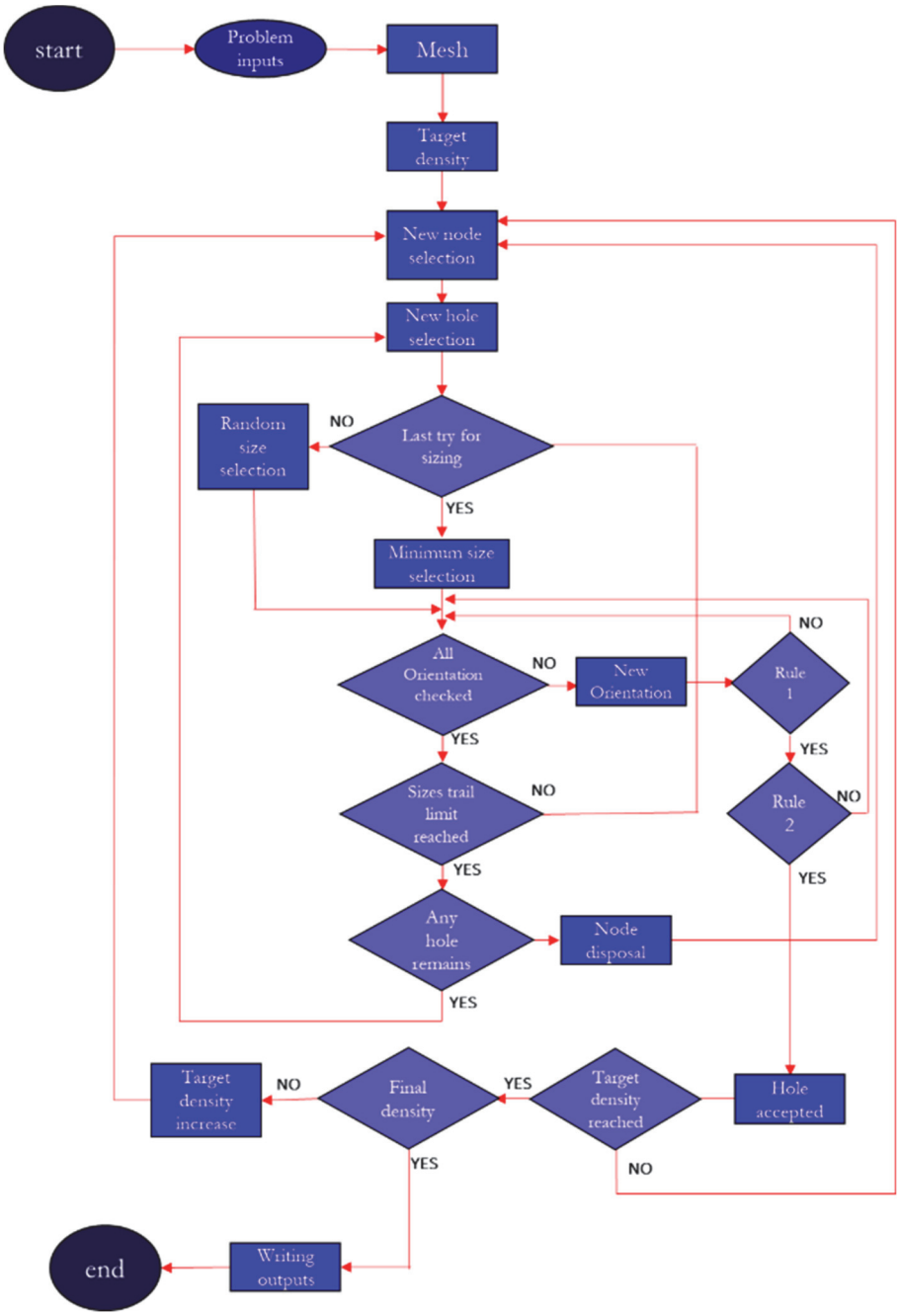

Figure 3: Flowchart of the porous body generation algorithm.

Porous Material CAD file output

The output of the second MATLAB code is a .txt files that contain the problem constraints such as the dimension of the geometry, and the void density of the geometry and it also has information on valid pores. The information needed to create this geometry are : 1- the ID of the used hole in the library, 2- the position of this hole, 3- the scale factor, and 4- the orientation angel.

The process of creating a porous geometry is a repetitive process so we can use micro writing and scripting to increase the speed and accuracy of generation. Here we use Abaqus software and scripting technique to achieve this goal. Based on the second MATLAB code output file, the geometry of the needed hole import as a sketch in Abaqus software. After the creation of the main geometry each hole is scaled, rotated, and translate to its correct position and this hole subtract from the previous geometry. This process can be done by any other CAD software as well. Fig. 4.a show the output of the cad file and Fig. 4.b represent its 3D form to comparison.

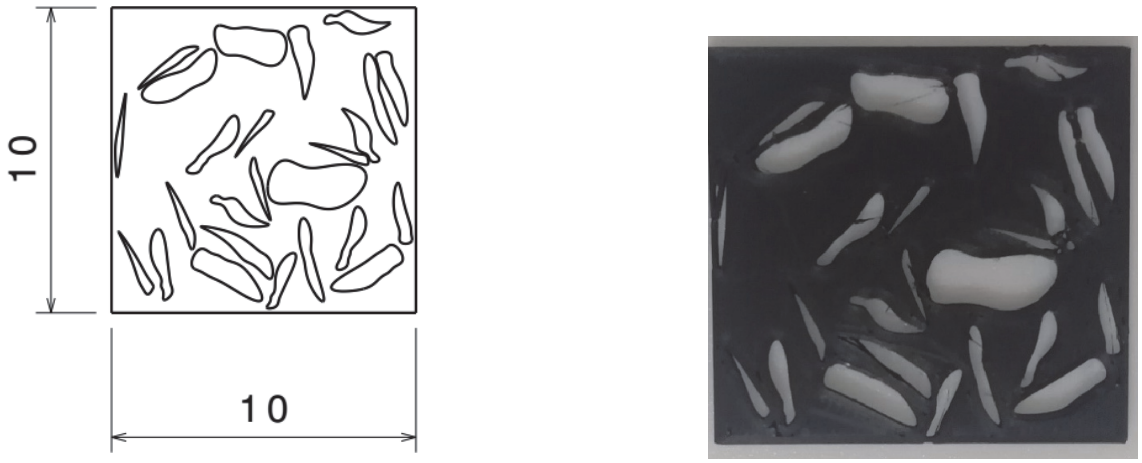

a. CAD output of the(mm) b. 3D printed output

Figure 4: Comparison between CAD file output and printed output.

Material and manufacturing method

Additive manufacturing is a production technique that allows the creation of three-dimensional objects by layering materials, such as plastics, metals, and ceramics, one thin layer at a time. The main different aspect of this method from the traditional method is that with additive manufacturing, the body is not subtracting from a larger block or piece, so the material waste and production cost will be significantly reduced. Besides that, this method makes it possible to create complex geometries and customized designs that would be difficult or even impossible to produce with traditional manufacturing methods.

FDM is one of the branches of additive manufacturing widely used today [19]. This method has many advantages, like low initial investment, ease of maintenance, and a wide range of materials that can be used. This method makes printing polymers, composites with short and long fibers, and nanocomposites possible [20].

The schematic picture of the printer is shown in Fig. 5. This device consists of four main parts, (1) Nozzle, (2) Extruder, (3) Heat Bed, and (4) Structure and Mechanisms. The extruder of These printers generally has 3 degrees of freedom (DOF) and can move through X, Y, and Z directions. Still, in some printers, the extruder is limited to X and Y directions, and the heat bed move vertically.

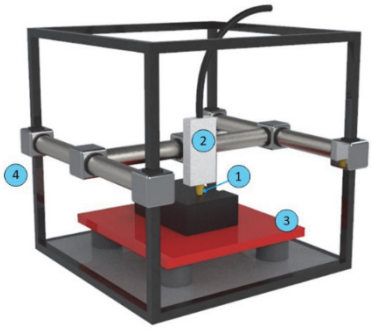

Figure 5: The schematic representation of components of common FDM printers.

In the FDM method, the thermoplastic filament is melted and extruded through the nozzle onto a build plate to create a three-dimensional object. This process begins with a 3D CAD model sliced by specialized software. The printer reads the file and moves the nozzle along the X, Y, and Z axes to deposit the material layer by layer. The filament is heated to a temperature specified by material type and determined in the output file of the slicer software. As each layer is deposited, it cools and solidifies, creating a solid bond with the previous layer. This process will continue until the entire object is complete. A simplified process flowchart of FDM is shown in Fig. 6.

Figure 6: simplified process flowchart of FDM.

Thermoplastic polymers are one group of materials that can be used in the FDM method. These polymers are typically well known, and this advantage brings many choices. Acrylonitrile butadiene styrene (ABS), polylactic acid (PLA), Nylon/polyamide, acrylonitrile styrene acrylate (ASA), polyethylene terephthalate (PET), polyethylene terephthalate glycol-modified (PETG) and polycarbonate (PC) are some of the thermoplastic filaments that commonly used in this method [21]. Each of these polymers has unique properties that could be used for particular tasks. In this work, we employed PLA with short carbon fiber chopped. PLA has high tensile strength and can easily degrade [22], and carbons fiber can improve the pure polymer's weak strength [23]. The microscopic image of the part of the sample is shown in Fig. 6. The fibers have random distribution in the matrix.

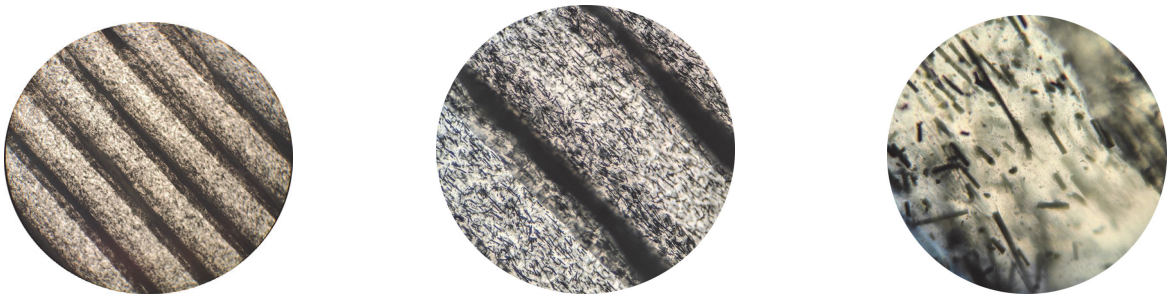

a. ×10 magnified b. ×40 magnified c. ×100 magnified

Figure 7: Short carbon fiber in PLA used in this paper.

The mechanical properties of the 3D-printed body are highly dependent on processing parameters. The main printing parameters are layer height, printing temperature, nozzle diameter, printing orientation, and printing speed [24,25]. Besides that, the nozzle's material, raster width, number of layers, and infill model can also be important.

Process parameter	Value	Unit
Nozzle diameter	0.4	mm
Nozzle temperature	235	° C
Bed temperature	60	° C
Infill	100 %	-
Printer speed	25	mm/s
Layer thickness	0.125	mm

Table 1: Process parameters for manufacturing test specimens.

Test specimen and test setups

The test specimens were fabricated via FDM using a Keytec M220 printer, and the G-code of the specimen was extracted with the help of the slicer Ultimaker® Cura 5.1.1. The process parameters for producing the test specimens are provided in Tab. 1. The PLA containing chopped short carbon fiber filament was used with a diameter of 1.75 mm. In this work, two types of specimens were fabricated; no-porous and porous. These specimens were produced based on type I of the ASTM D638-14 standard with a thickness of 2mm. The no-porous specimens were fabricated with two orientations [0], [90] separately to investigate the mechanical properties of the filament based on selected print parameters (see Fig. 8).

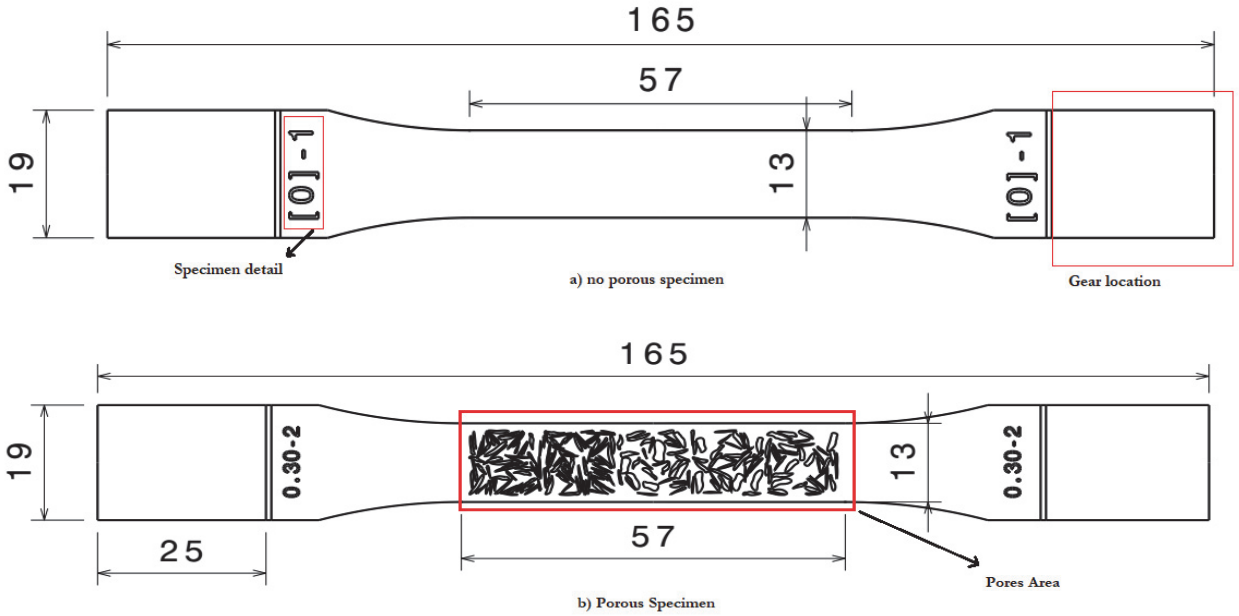

Figure 8: Schematic examples illustration of (a) no porosity and (b) porous specimens.

Each specimen consists of 16 layers and the orientation in all of them is the same. Also, the orientation of the raster is calculated from the loading direction which we assume that the [0] direction is the case that the loading vector is along the raster angle, and for [90] orientation this vector is perpendicular to the raster angle. Fig. 9 shows the slicing output and the reference axis system for the specimens.

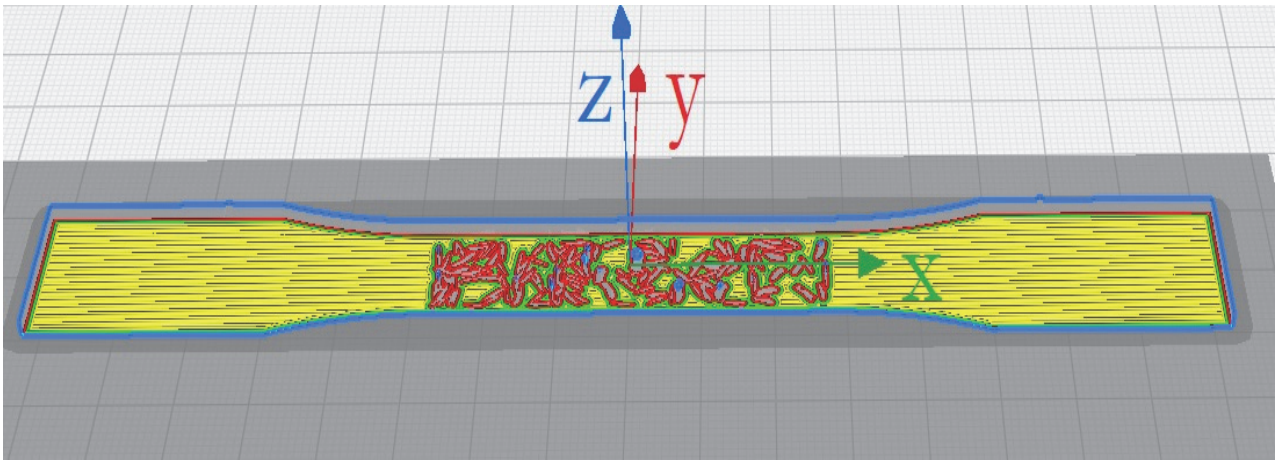

Figure 9: Slicing output from Ultimaker® Cura 5.1.1 .

In the porous specimens, the pores were located at the center of the specimen. In total, seven porous specimens were produced with porosity of 0.05 to 0.40 with the step of 0.05, as shown in Fig. 10. Because of the limitation created by nozzle diameter, this work can't achieve specimens with higher porosity. Also, because the porous material's properties depend on the loading direction, the direction of the specimens is specified on the specimens with the grip location, and specimen labels are all by printing in both types of specimens. The orientation of the porous specimens is [0].

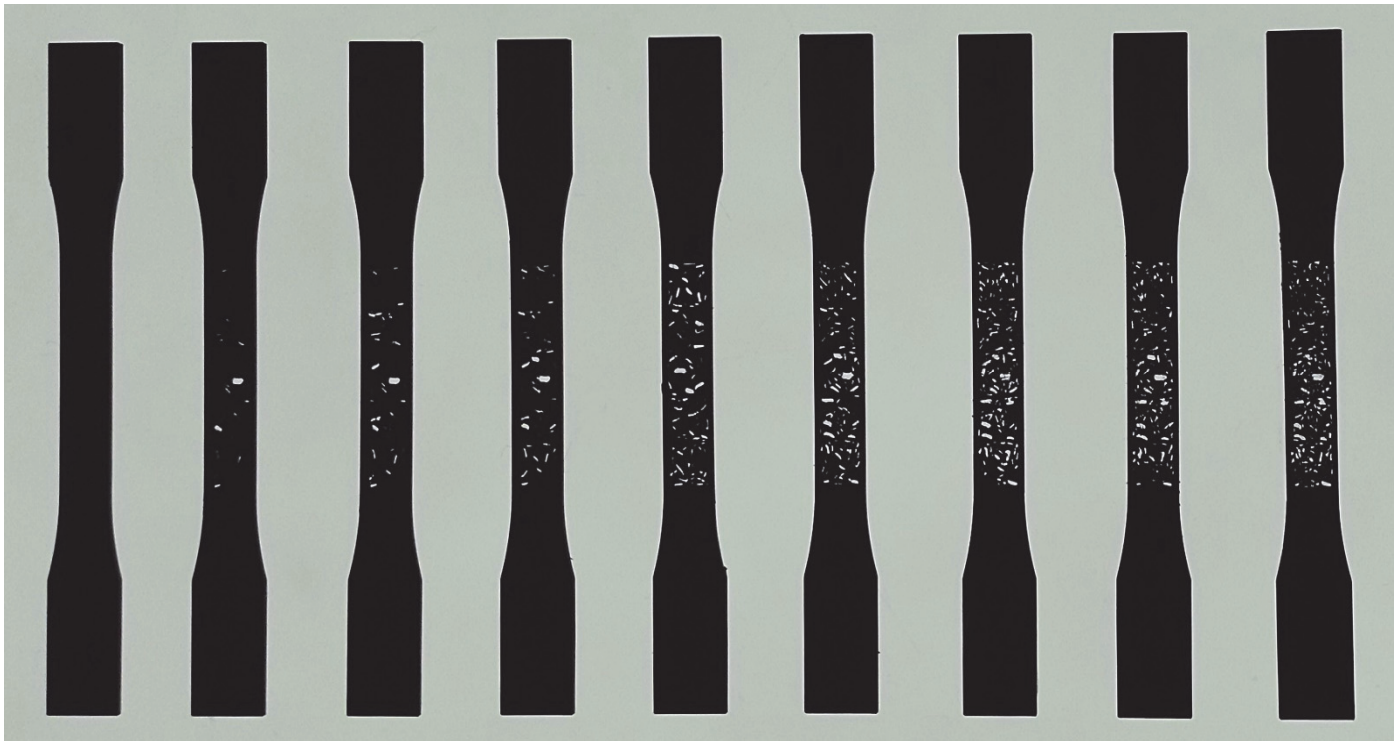

Figure 10: Porous specimens.

Tensile tests were carried out to extract stress-strain curves, employing a universal tension–compression testing machine at a displacement rate of 1 mm/min. All quasi-static tests were carried out at room temperature under displacement control. The stress was estimated by dividing the load by the specimens' cross-section and the strain by dividing the displacement by the length between gears. Three specimens were tested for each set of manufacturing parameters. The reported results are the average values.

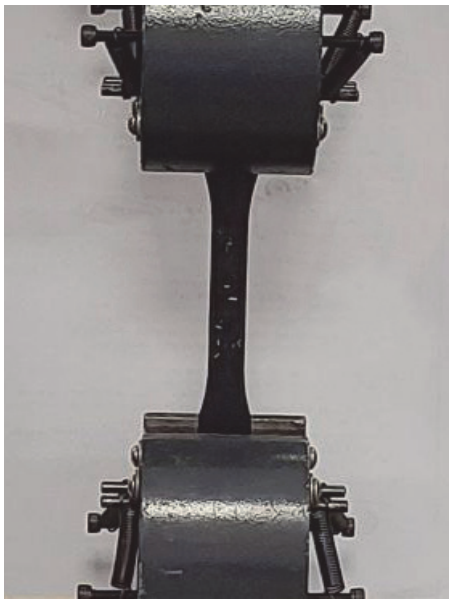

Figure 11: Test setup for specimens on SANTAM universal tension-compression testing machine.

The output stress-strain curve for set 1 of the specimens is shown in Fig. 12. Two response variables can evaluate with these results, elastic modulus (E) and Maximum Tensile Stress (MTS). These parameters can describe the material's tensile

properties and the effect of porosity. Effective elastic modulus measures the rigidity or stiffness of the material in the presence of porosity. It is the stress ratio to the corresponding strain but below the proportionality limit.

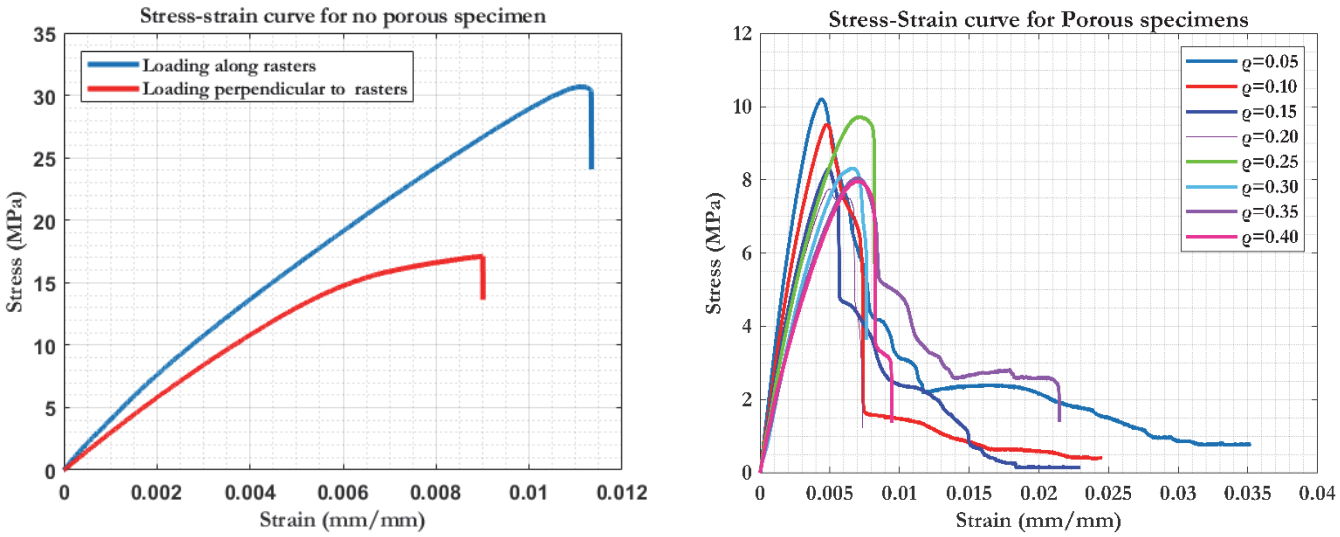

a.no porosity specimens b. porous specimen

Figure 12: The stress-strain curves for the set I of the specimens.

Fig. 12. a represents the stress-strain response of the no-porosity specimen aligned and perpendicular to the raster angle. The orthotropic behavior of the body fabricated by FDM can be seen in this figure because of the overlapping of this raster. But this overlapping won't act as fiber reinforcement in composites, and this material cannot be categorized as highly orthotropy. Also, Fig. 12. b shows the effect of the different porosities on mechanical properties for one set of specimens. The ultimate stress and young's modulus decrease with the increased porosity. Besides that, the long damage zone after the ultimate stress is interesting.

THEORY OF THE PROBLEM

To investigate the effect of porosity on the orthotropic material's mechanical properties, we consider an RVE that describes the general form of this material. Fig. 13 shows that this RVE can be discrete into two phases.

The orthotropic behavior of the materials produced by the FDM technique is because of the raster angle and overlapping of this raster (see Fig. 7). it is possible to assume that these narrow lines (created by overlapping) carry some of the force applied, like what fibers do in composites.

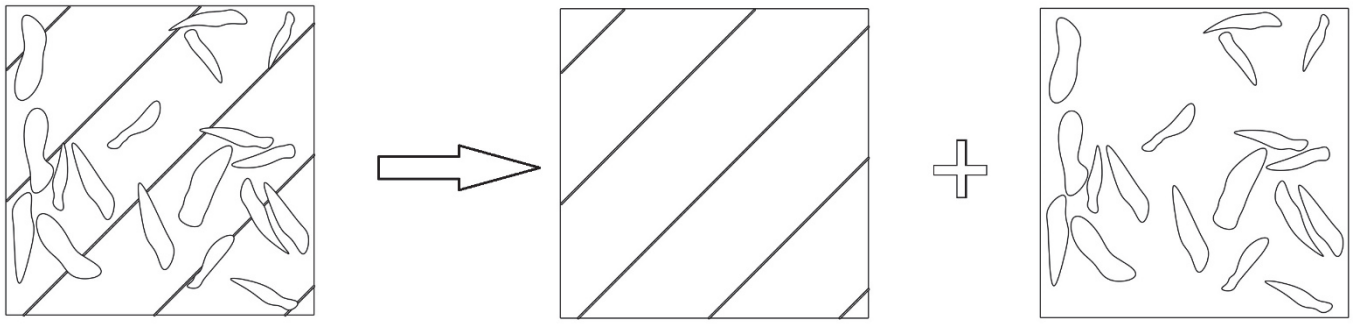

a. Represented Volume Element b. orthotropic phase c. porous phase

Figure 13: Represented Volume Element (RVE) for porous material produced by the FDM technique.

So based on the RIS concept, we consider these orthotropic materials as isotropic ones which have reinforced and encounter the effect of these reinforcements on the stress that is applied to the RVE. This reduction in applied stress calculates by using "reinforcement factors" that are defined below mathematically:

$$\sigma_{xx}^{Matrix} = \sigma_{xx}^{Comp.} / n_1 \tag{1}$$

$$\sigma_{yy}^{Matrix} = \sigma_{yy}^{Comp.} / n_2 \tag{2}$$

$$\sigma_{xy}^{Matrix} = \sigma_{xy}^{Comp.} / n_6 \tag{3}$$

where $\sigma_{ij}^{Comp.}$ is the stress applied to the composite material, and σ_{ij}^{Matrix} is the portion of stress reduced by the reinforcements. The reinforcement factor can find with a combination of equilibrium and constitutive relations with compatibility equations for isotropic matrix. The constitutive relation for orthotropic materials is:

$$\varepsilon_x = \frac{\sigma_x}{E_x} - \frac{\nu_{xy}\sigma_y}{E_y} \tag{4}$$

$$\varepsilon_y = \frac{\sigma_y}{E_y} - \frac{\nu_{yx}\sigma_x}{E_x} \tag{5}$$

$$\gamma_{xy} = \frac{\tau_{xy}}{G_{xy}} \tag{6}$$

with the definition of Airy stress function, we have:

$$\sigma_x = \frac{\partial^2 \varphi}{\partial y^2} \tag{7}$$

$$\sigma_y = \frac{\partial^2 \varphi}{\partial x^2} \tag{8}$$

$$\tau_{xy} = -\frac{\partial^2 \varphi}{\partial x \partial y} \tag{9}$$

The compatibility equation for isotropic material can be written as follows:

$$\frac{\partial^2 \varepsilon_x}{\partial y^2} + \frac{\partial^2 \varepsilon_y}{\partial x^2} = \frac{\partial^2 \gamma_{xy}}{\partial x \partial y} \tag{10}$$

So, with the placement of Eq. (4-6) into Eq. (7-9) and substituting the result into the compatibility equation, and using constitutive relations, we have:

$$C_{22}\frac{\partial^4 \varphi}{\partial x^4} + (C_{66} + 2C_{12})\frac{\partial^4 \varphi}{\partial x^2 \partial y^2} + C_{11}\frac{\partial^4 \varphi}{\partial y^4} = 0 \tag{11}$$

where C_{ij}'s are the components of the compliance matrix. In orthotropic material with a Cartesian coordinate system, this matrix can be written as:

$$\begin{bmatrix} \varepsilon_x \\ \varepsilon_y \\ \varepsilon_z \\ \gamma_{yz} \\ \gamma_{zx} \\ \gamma_{xy} \end{bmatrix} = \begin{bmatrix} \frac{1}{E_x} & \frac{-\nu_{yx}}{E_y} & \frac{-\nu_{zx}}{E_z} & 0 & 0 & 0 \\ \frac{-\nu_{xy}}{E_x} & \frac{1}{E_y} & \frac{-\nu_{zy}}{E_z} & 0 & 0 & 0 \\ \frac{-\nu_{xz}}{E_x} & \frac{-\nu_{yz}}{E_y} & \frac{1}{E_z} & 0 & 0 & 0 \\ 0 & 0 & 0 & \frac{1}{G_{yz}} & 0 & 0 \\ 0 & 0 & 0 & 0 & \frac{1}{G_{zx}} & 0 \\ 0 & 0 & 0 & 0 & 0 & \frac{1}{G_{xy}} \end{bmatrix} \begin{bmatrix} \sigma_x \\ \sigma_y \\ \sigma_z \\ \tau_{yz} \\ \tau_{zx} \\ \tau_{xy} \end{bmatrix} \tag{12}$$

For plane stress conditions in the x-y plane, only the C_{11}, C_{22}, C_{12}, C_{21}, and C_{66} will remain. The components of this matrix are constant, and the matrix is symmetric. For - plane strain cases, four components of this matrix should be changed as below:

$$C_{ij}' = C_{ij} - C_{i3}C_{j3} / C_{33} \qquad (i, j = 1,2) \tag{13}$$

To include the effect of the reinforcement factor, we repeat the previous procedure with a slight change. This time we are using Eq. (1-3) Instead of Eq. (7-9), and the result can be written as [26]:

$$C_{22}\frac{\partial^4 \varphi}{\partial x^4} + (n_6 C_{66} + (1+n_1)C_{12})\frac{\partial^4 \varphi}{\partial x^2 \partial^2 y} + n_1 C_{11}\frac{\partial^4 \varphi}{\partial y^4} = 0 \tag{14}$$

The reinforcement factor should have also followed the below configuration to be used as isotropic material.

$$n_1 = \frac{C_{22}}{C_{11}} = \frac{E_x}{E_y} \tag{15}$$

$$n_6 = \left(2 - \frac{C_{12}}{C_{22}} - \frac{C_{12}}{C_{11}}\right)\frac{C_{22}}{C_{66}} = (2 + \nu_{yx} + \nu_{xy})\frac{G_{xy}}{E_y} \tag{16}$$

For a cracked orthotropic material generalized elastic moduli defined as [27]:

$$E_I = \left[\frac{C_{11}C_{22}}{2}\left(\sqrt{\frac{C_{22}}{C_{11}}} + \frac{2C_{12} + C_{66}}{2C_{11}}\right)\right]^{-1/2} \tag{17}$$

$$E_{II} = \left[\frac{C_{11}^{\ 2}}{2}\left(\sqrt{\frac{C_{22}}{C_{11}}} + \frac{2C_{12} + C_{66}}{2C_{11}}\right)\right]^{-1/2} \tag{18}$$

With this result, generalized elastic moduli will have the following form [28]:

$$E_I = \left[\frac{1}{2E_x E_y} \left(\sqrt{n_1} - \nu_{12} + \frac{n_1}{2n_6}(2 + \nu_{21} + \nu_{12}) \right) \right]^{-\frac{1}{2}} \tag{19}$$

$$E_{II} = \left[\frac{1}{2E_x{}^2} \left(\sqrt{n_1} - \nu_{12} + \frac{n_1}{2n_6}(2 + \nu_{21} + \nu_{12}) \right) \right]^{-\frac{1}{2}} \tag{20}$$

Several studies have been made to calculate the effect of the pores and micro-cracks on the material's overall properties. The porous materials are load-induced anisotropic, i.e., mechanical properties depend on the load pass. However, if all the pores are all open and have a random distribution, they can assume as isotropic [4]. Budiansky and O'Connell have obtained the effective elastic moduli of a body containing open micro-crack. For a solid containing uncorrelated pores, we have [8]:

$$\frac{\bar{E}}{E} = 1 - \frac{2N\langle a^3 \rangle}{15} \left[3\langle f(\bar{\nu}) \rangle + 2\langle g(\bar{\nu}, \psi) \rangle \right] \tag{21}$$

$$\frac{\bar{K}}{K} = 1 - \frac{2N\langle a^3 f(\bar{\nu}) \rangle}{3(1 - 2\bar{\nu})} \tag{22}$$

$$1 - \frac{\bar{G}}{G} - \frac{3\bar{G}}{\bar{E}} \left(1 - \frac{\bar{E}}{E} \right) - \frac{\bar{G}}{3\bar{K}} \left(1 - \frac{\bar{K}}{K} \right) = 0 \tag{23}$$

where $\bar{E}, \bar{K}, \bar{G}, \bar{\nu}$ are effective elastic modulus bulk modulus, shear modulus, Poisson's ratio respectively, $f(\bar{\nu})$ and $g(\bar{\nu}, \psi)$ represent the shape coefficient that defined based on pores geometry, N is the number of pores per unit volume and the symbol . calculates the mean value. For narrow elliptical pores, these shape coefficients are defined as follows [8]:

$$f(\bar{\nu}) = \left(\frac{4\pi}{3} \right) \left(\frac{b}{a} \right)^2 \left(\frac{1 - \bar{\nu}^2}{E(k)} \right) \tag{24}$$

$$g(\bar{\nu}, \psi) = \frac{4\pi}{3} \left(\frac{b}{a} \right)^2 \left(1 - \bar{\nu}^2 \right) \left[R(k, \bar{\nu}) \cos^2 \psi + Q(k, \bar{\nu}) \sin^2 \psi \right] \tag{25}$$

$$k = (1 - b^2 / a^2)^{1/2} \tag{26}$$

where a and b are major and minor axes of the considered ellipse. Q and R are complete elliptic integrals of the first kind with argument k. effective elastic modules for material extracted as follow [8]:

$$\frac{\bar{E}}{E} = 1 - \frac{16}{45}(1 + \bar{\nu})(5 - 4\bar{\nu})\rho \tag{27}$$

$$\frac{\bar{G}}{G} = 1 - \frac{8}{45}(10 - 7\bar{\nu})\rho \tag{28}$$

where ρ is micro-crack density parameter and calculate as follows [8]:

$$\rho = \frac{45}{8}\frac{\nu - \bar{\nu}}{(1+\bar{\nu})\left[10\nu - \bar{\nu}(1+8\nu)\right]} \tag{29}$$

The Denominator of the left-hand side of Eqns. 27 and 28 must choose wisely in orthotropic material. Here we suggest two relations to check with experimental results. One of them is to assume that effective elastic moduli of each direction are obtained just from its direction properties. It means:

$$\bar{E}_i = E_i\left[1 - \frac{16}{45}(1+\bar{\nu})(5-4\bar{\nu})\rho\right] \qquad (i=1,2) \tag{30}$$

The other relation used generalized elastic moduli that have been rewritten by RIS assumption Eqns. (19 & 20) as Denominator, so:

$$\bar{E}_1 = E_I\left[1 - \frac{16}{45}(1+\bar{\nu})(5-4\bar{\nu})\rho\right] \tag{31}$$

$$\bar{E}_2 = E_{II}\left[1 - \frac{16}{45}(1+\bar{\nu})(5-4\bar{\nu})\rho\right] \tag{32}$$

The compression between these two relations has been discussed in the next section.

RESULT AND DISCUSSION

With the stress-strain curves, it is possible to calculate the mechanical properties of the specimens. The average value of the elastic modulus and ultimate stress is described in Tab. 2. As we expect, these values will decrease with increased porosity.

Porosity (A_{voids} / A_{total})	Elastic Modulus (MPa)	Ultimate stress (MPa)
0 (along raster)	3.808	30.675
0 (pre. to raster)	2.8993	17.1112
0.05	2.9385	10.2062
0.10	2.6822	9.7158
0.15	2.3157	9.5081
0.20	2.1451	8.3196
0.25	1.8271	8.3008
0.30	1.6481	8.0365
0.35	1.4103	7.9612
0.40	1.2660	7.7538

Table 2: Average value of the Elastic modulus and Ultimate stress extracted from the test based on porosity.

Based on the experimental and curve fitting, a polynomial relation is represented here to describe the effective elastic modulus along the raster.

$$\bar{E}_i = E_i(1 - n\rho) \tag{33}$$

where ε is void density and n is a material factor that could have a different value in various materials, here this value is equal to 1.85 for the body that generates with PLA contains short fiber carbon with print parameter described in Tab. 1, and loading along raster loading. The result of eq 33 is very close to eq 30. Fig. 14 shows the fitted equation and two other theoretical relations (eq 30 & eq 31) plotted with the experimental data. The result of Eqn. 31, based on RIS theory and generalized elastic moduli, agrees better with the experimental findings.

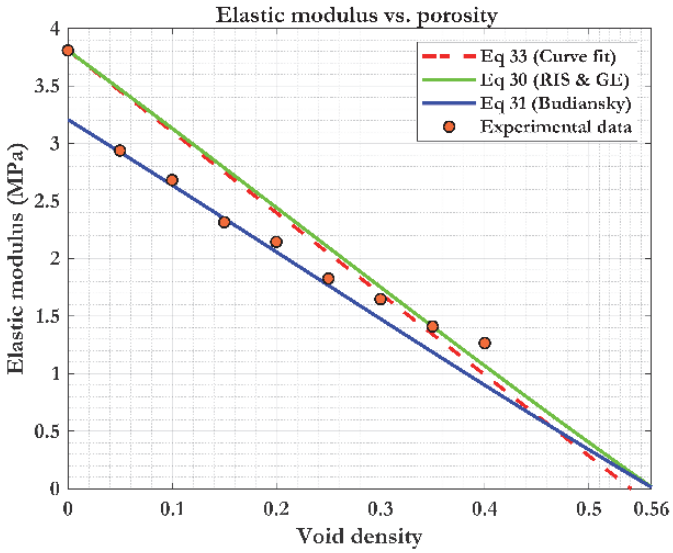

Figure 14: Represented Volume Element (RVE) for porous material produced by the FDM technique.

The porous specimens have the same base, meaning the porosity increases by adding new holes to the previous porosity state. However, the fracture behaviors for this material change a lot. Some specimens experience catastrophic failure, but others break at two or more locations and experience large intervals of nonlinearity, like specimens with a porosity of 0.05(see Fig. 15. b). these phenomena are out of the scope of this paper. Some examples of the Fracture of these specimens show in Fig. 15. The specimen shown in Fig. (15.a) has several breakpoints, and its fracture is similar to plastic materials; conversely, the specimen whit porosity of 0.25 has a catastrophic failure and acts like a brittle material.

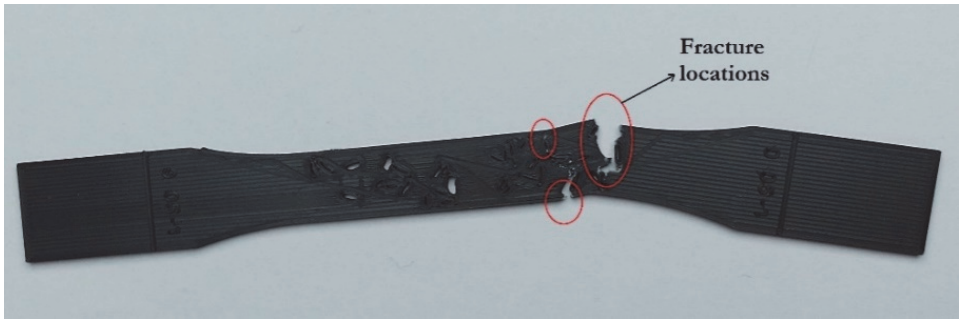

a. specimen with porosity of 0.05

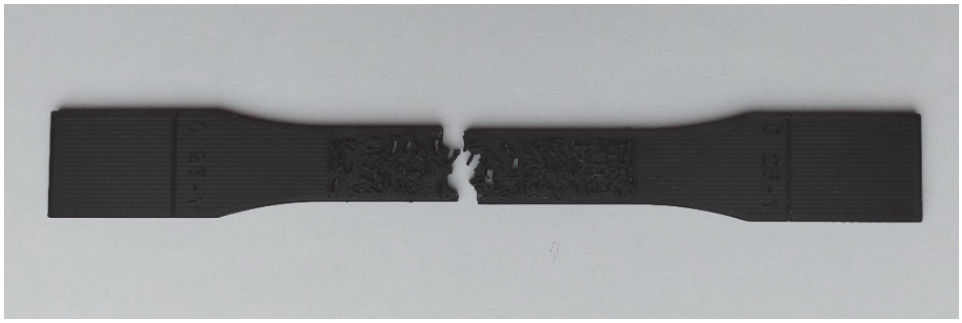

b. specimen with porosity of 0.25

Figure 14: Examples of Fracture behaviors of the porous body.

Conclusions

The purpose of this work was an investigation the pores of mechanical properties of porous materials produced with FDM 3D printing. Two types of specimens were fabricated, porous and no porosity material. With the help of the tensile test and extracted stress-strain curve, elastic modulus and maximum tensile stress for different porosity were evaluated. A polynomial equation is represented based on the experimental results and curve fitting (eq 33).

Also, with Represented Volume Element (RVE) represented in this work, the porous 3D printed body is discrete to an orthotropic and porous phase. The porous phase is isotropic [9], and generalized elastic moduli were calculated for the orthotropic phase with the help of RIS modeling and using reinforcement factors. The combination of existing isotropic effective properties and RIS theory, a theoretical expression derived for an orthotropic porous material. The experimental outcomes closely match those predicted by the theoretical framework.

As described, the specimen's location and shape of fracture change in different porosity. This material's nonlinearity and fracture process are of significant interest, and we plan to conduct further research to understand its properties in the future better. Also, in this work, we use a section of the general porous material for investigation. So, the effect of the pore's shape on the whole material might not determine very well. Using other modification methods for pores in modeling a random 3D porous material can be a good topic for achieving a better understanding of these materials' general behaviors.

References

[1] Vafai, K. (2010). Porous media: applications in biological systems and biotechnology, CRC press.
[2] Mujeebu, M.A., Abdullah, M.Z., Bakar, M.Z.A., Mohamad, A.A., Abdullah, M.K. (2009). Applications of porous media combustion technology–a review, Appl. Energy, 86(9), pp. 1365–1375.
[3] Sun, M.-H., Huang, S.-Z., Chen, L.-H., Li, Y., Yang, X.-Y., Yuan, Z.-Y., Su, B.-L. (2016). Applications of hierarchically structured porous materials from energy storage and conversion, catalysis, photocatalysis, adsorption, separation, and sensing to biomedicine, Chem. Soc. Rev., 45(12), pp. 3479–3563.
[4] Leguillon, D., Piat, R. (2008). Fracture of porous materials–Influence of the pore size, Eng. Fract. Mech., 75(7), pp. 1840–1853.
[5] Glodež, S., Dervaric, S., Kramberger, J., Šraml, M. (2016). Fatigue crack initiation and propagation in lotus-type porous material, Frat. Ed Integrità Strutt., 10(35), pp. 152–160.
[6] Kramberger, J., Sterkuš, K., Glodež, S. (2016). Damage and failure modeling of lotus-type porous material subjected to low-cycle fatigue, Frat. Ed Integrità Strutt., 10(35), pp. 142–151.
[7] Skorokhod, V. V. (1967). Some physical properties of high-porosity bodies, Sov. Powder Metall. Met. Ceram., 6, pp. 453–457.
[8] Budiansky, B., O'connell, R.J. (1976). Elastic moduli of a cracked solid, Int. J. Solids Struct., 12(2), pp. 81–97.
[9] Horii, H., Nemat-Nasser, S. (1983). Overall moduli of solids with microcracks: load-induced anisotropy, J. Mech. Phys. Solids, 31(2), pp. 155–171.
[10] Sevostianov, I., Kushch, V. (2009). Effect of pore distribution on the statistics of peak stress and overall properties of porous material, Int. J. Solids Struct., 46(25–26), pp. 4419–4429.
[11] Chakraborty, A. (2011). An analytical homogenization method for heterogeneous porous materials, Int. J. Solids Struct., 48(24), pp. 3395–3405.
[12] Quintanilla, J., Torquato, S. (1997). Microstructure functions for a model of statistically inhomogeneous random media, Phys. Rev. E, 55(2), pp. 1558.
[13] Kushch, V.I., Shmegera, S. V., Mishnaevsky Jr, L. (2008). Meso cell model of fiber reinforced composite: interface stress statistics and debonding paths, Int. J. Solids Struct., 45(9), pp. 2758–2784.
[14] Christensen, R.M., Freeman, D.C., DeTeresa, S.J. (2002). Failure criteria for isotropic materials, applications to low-density types, Int. J. Solids Struct., 39(4), pp. 973–982.
[15] Joffre, T., Chen, S., Isaksson, P. (2016). Microscopic strain fields at crack tips in porous materials analyzed by a gradient-enhanced elasticity theory, Eng. Fract. Mech., 168, pp. 160–173.
[16] Joshi, S.C., Sheikh, A.A. (2015). 3D printing in aerospace and its long-term sustainability, Virtual Phys. Prototyp., 10(4), pp. 175–185.
[17] Richardson, M., Haylock, B. (2012). Designer/maker: the rise of additive manufacturing, domestic-scale production and the possible implications for the automotive industry, Comput. Des. Appl. PACE, 2, pp. 33–48.
[18] Wickramasinghe, S., Do, T., Tran, P. (2020). FDM-based 3D printing of polymer and associated composite: A review

on mechanical properties, defects and treatments, Polymers (Basel)., 12(7), pp. 1529.
[19] Turner, B.N., Strong, R., Gold, S.A. (2014). A review of melt extrusion additive manufacturing processes: I. Process design and modeling, Rapid Prototyp. J., 20(3), pp. 192–204.
[20] Mohan, N., Senthil, P., Vinodh, S., Jayanth, N. (2017). A review on composite materials and process parameters optimisation for the fused deposition modelling process, Virtual Phys. Prototyp., 12(1), pp. 47–59.
[21] Mazzanti, V., Malagutti, L., Mollica, F. (2019). FDM 3D printing of polymers containing natural fillers: A review of their mechanical properties, Polymers (Basel)., 11(7), pp. 1094.
[22] Elsawy, M.A., Kim, K.-H., Park, J.-W., Deep, A. (2017). Hydrolytic degradation of polylactic acid (PLA) and its composites, Renew. Sustain. Energy Rev., 79, pp. 1346–1352.
[23] Ferreira, I., Machado, M., Alves, F., Torres Marques, A. (2019). A review on fibre reinforced composite printing via FFF, Rapid Prototyp. J., 25(6), pp. 972–988.
[24] Marsavina, L., Vălean, C., Mărghitaş, M., Linul, E., Razavi, S.M.J., Berto, F., Brighenti, R. (2022). Effect of the manufacturing parameters on the tensile and fracture properties of FDM 3D-printed PLA specimens, Eng. Fract. Mech., 274, pp. 108766.
[25] Torres, J., Cole, M., Owji, A., DeMastry, Z., Gordon, A.P. (2016). An approach for mechanical property optimization of fused deposition modeling with polylactic acid via design of experiments, Rapid Prototyp. J., 22(2) pp. 387-404.
[26] Van der Put, T. (2007). A new fracture mechanics theory for orthotropic materials like wood, Eng. Fract. Mech., 74(5), pp. 771–781.
[27] Sih, G.C. (1974). Strain-energy-density factor applied to mixed mode crack problems, Int. J. Fract., 10, pp. 305–321.
[28] Fakoor, M. (2017). Augmented strain energy release rate (ASER): A novel approach for investigation of mixed-mode I/II fracture of composite materials, Eng. Fract. Mech., 179, pp. 177–189.